Experimental analysis of the ICRF waves coupling in EAST

J.H. Zhang[1,2], X.J. Zhang[1*], Y. Cheng[1*], C.M. Qin[1], Y.P. Zhao[1], Y.Z. Mao[1], S. Yuan[1], L. Wang[1], S.Q. Ju[1], G. Chen[1], B.N. Wan[1], X.Z. Gong[1], J.P. Qian[1], T. Zhang[1], J.H. Wu[1], J.G. Li[1], Y.T. Song[1], Y.Q. Yang[1,2], Z. Chen[1,2], J.H. Wang[1,2], Y. Lin[3], G. Taylor[4], S. Wukitch[3], J.M. Noterdaeme[5,6], J.C. Hosea[4], R. Kumazawa[7], T. Seki[7], K. Saito[7] and H. Kasahara[7]

[1] Institute of Plasma Physics, Chinese Academy of Sciences, Hefei 230031, People's Republic of China

[2] University of Science and Technology of China, Hefei 230026, People's Republic of China

[3] MIT Plasma Science and Fusion Center, Cambridge, MA 02139, USA

[4] Princeton Plasma Physics Laboratory, Princeton, NJ 08543, USA

[5] Max-Planck Institute for Plasma Physics, D-85748, Garching, Germany

[6] EESA Department, University of Gent, B-9000 Gent, Belgium

[7] National Institute for Fusion Science, Toki, 509-5292 Japan

* E-mail: xjzhang@ipp.ac.cn and chengy@ipp.ac.cn

Abstract. The experiments were carried out to study the coupling characteristics of the I-port antenna in the ion cyclotron range of frequencies (ICRF) in EAST. The dependencies of the coupling resistance on various parameters including the antenna position, the central electron density, gas injection and the antenna phasing have been studied. The results obtained show that the experimental data are consistent with theoretical simulations. We find that the antenna loading resistance decreases sharply at the L-H transition due to the change of the plasma density profiles in the scrape-off layer (SOL). The effect of the low hybrid wave (LHW) on the ICRF coupling during the H-mode is observed. The theoretical interpretation of the results is discussed, together with the efficient methods to optimize the coupling efficiency.

Keywords: ICRF, Coupling, EAST

PACS: 52.50.Qt, 52.35.Hr, 52.25.Os, 52.55.Fa

1.Introduction

Using the fast magnetosonic wave in ion cyclotron range of frequencies (ICRF) to heat ions and electrons in the plasma core efficiently has been demonstrated in EAST［1,2］and other tokamaks［3-5］. The newly designed and installed ICRF antenna in I port aiming at increasing the ICRF heating efficiency has been analyzed theoretically in Ref. [6]. The ICRF antenna array which consists of 4 straps can operate in various heating and current drive phasing cases in 25~70MHz. In this paper, we report the study of the ICRF coupling characteristics of the I-port antenna from recent experiments performed on EAST.

Plenty of factors have influences on the ICRF antenna coupling and various experiments have been carried out to study the dependence of the coupling on these factors in a number of devices. Quantitative agreement between the theoretical and experimental dependence of the antenna loading resistance on the various plasma parameters has been obtained in DIII-D [7]. The loading resistance showed a clear increase with the increasing line average electron density close to the plasma edge during gas injection experiments in TEXTOR [8]. On Alcator C-Mod, the antenna loading was found to be sensitive to the plasma density profile in

the SOL and pedestal [9]. The performance of three different dipole phasing configurations is assessed experimentally by using the JET A2 ICRF antennas [10]. The experimental resonant behaviour of the loading resistance in ASDEX due to the variation of the density is explained reasonably by the eigenmode effect [11]. This paper presents the first study of the ICRF antenna coupling vs. various plasma parameters on EAST tokamak.

The paper is organized as follows. The definition of the coupling resistance and the antenna code are described in Section 2. In Section 3, the dependencies of the loading upon various plasma parameters are analyzed. The coupling characteristic features of these discharges are also analyzed. The comparisons of the antenna loading with the theoretical simulations, using the antenna code are discussed in Sections 3. Finally, the conclusions are presented in Sections 4.

2. The antenna model and the definition of the coupling resistance

The relative positions of the ICRF antenna in I port and the magnetic connections at the position of the limiter are shown in Figure1(a). ϕ and θ are the toroidal and poloidal angle in degrees of the EAST tokamak respectively. The microwave reflectometry to measure the density profiles of the plasma is marked by the red square. The microwave reflectometry is in the mid-plane just beside the I port. The structures of the 1×4 antenna array in I port are shown in Figure1(b). The strap width and the separations between adjacent straps are all 100mm.

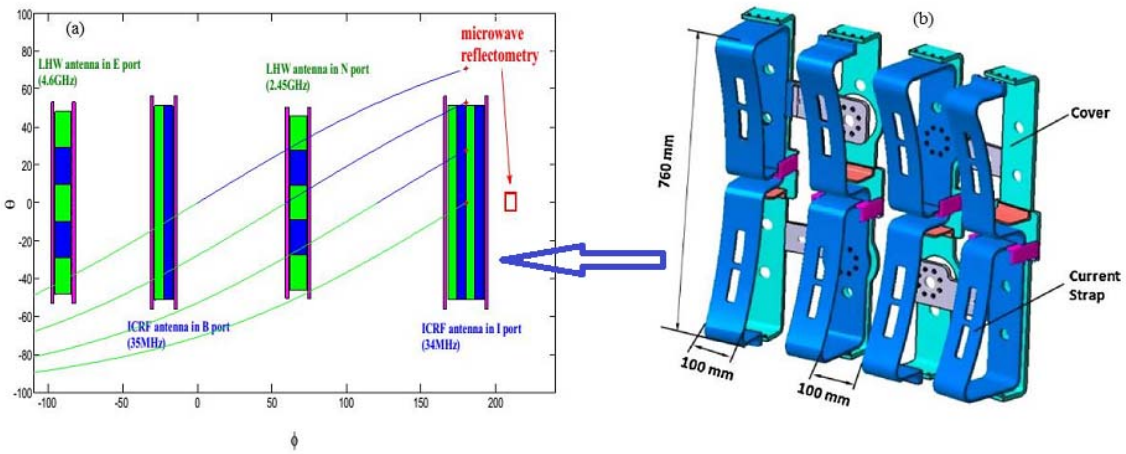

Figure 1. (a) The relative positions of the ICRF antenna in I port and the magnetic connections at the position of the limiter. ϕ and θ are the toroidal and poloidal angle in degrees of the EAST tokamak respectively. The red square represents the microwave reflectometry. (b) The structures of the 1×4 ICRF antenna array in I port.

2.1 The experimental coupling resistance

The experimental ICRF antenna coupling performance is evaluated as a coupling (or loading) resistance R_c defined by:

$$R_c = \frac{2P_{trans} \cdot Z_0^2}{V_{max}^2} \tag{1}$$

where P_{trans} is the power transmitted, V_{max} is the measured peak voltage in the coaxial line and Z_0 is the characteristic impedance of the transmission line. P_{trans} is equivalent to the power radiated by the antenna if we neglect the losses on the transmission line. P_{trans} is measured by the directional coupler in front of the transmitter and the V_{max} is given by the voltage probe on the transmission line. The final measurement error of the coupling resistance is less than 5%.

2.2 The theoretical coupling resistance

To analyze the coupling resistance theoretically, the ICRF antenna coupling code (antenna code) based on the variational theory [12] was employed. The antenna code has been upgraded with I-port antenna model [13]. The antenna structure and the schematic drawing of slab coupling model are shown in Figure 2. The Faraday shield and the plasma edge is located at the radial position $x = c$ and $x = d$, respectively. The antenna consists of two main radiating conductors at $x = b_2$ and two return conductors at $x = b_1$. The feeder point connects to the return conductors at $y = y_F$. The upper main radiating conductor shorts at $y = y_1$ and the lower main radiating conductor shorts at $y = -y_2$. The width of the conductors in the z-direction is w.

The plasma model takes into account the inhomogeneities of the density and the

magnetic field, present in a real tokamak plasma. The density profile used in calculations comes from the data measured by the microwave reflectometry in Figure 1. We assume that the power radiated by the antenna is sufficiently absorbed (imposing a radiation boundary condition at the plasma bulk $x = d + l_n$) and neglect the possibility of cavity resonances in the tokamak. The details of the derivation of the wave equations describing the folded antenna array are shown in appendix A. After the current distributions on the straps are determined by variational theory, the theoretical radiation resistance R_{rad} could be given as:

$$R_{rad} = \frac{\mathrm{Re}\int_D \boldsymbol{J}^* \cdot \boldsymbol{E}\mathrm{d}\boldsymbol{R}}{\left|I_S\right|^2} \tag{2}$$

where D denotes the surface of the current straps, $\boldsymbol{J}$ are the antenna currents, I_S is the maximum current value (at the short point) and the integral is over all current straps.

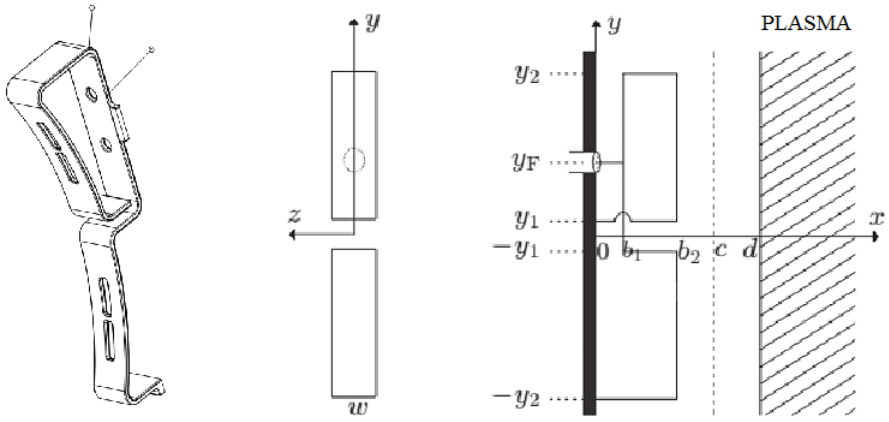

Figure 2. Geometry of the coupling model: (a) realistic antenna structure of one antenna strap in I port, (b) front view and (c) poloidal cross-sectional view for the single ICRF antenna. The *z* direction of the coordinate is parallel to toroidal magnetic field, the *y* direction is in the poloidal direction, and the *x* direction is in the radial direction pointing to the plasma.

After the radiation resistance R_{rad} is obtained, we could employ the circuit model to derive the input impedance Z_{in} at the antenna input terminal. Figure 3 gives the upper loop circuit model of the antenna [14], in which the transmission line is considered loss-less and lumped resistance R_{rad} at the short point accounts for the radiation. C_P represents the capacitive coupling of the return conductor and the back wall. Z_L gives the self-inductance of a part of the upper radiation conductor between the feeder and the shorter point. The input impedance of the upper loop Z_{in}^{upper} at the input terminal could be calculated easily:

$$Z_{in}^{upper} = \frac{Z_T + Z_L + R_{rad}}{1 - i\omega C_P (Z_T + Z_L + R_{rad})} \tag{3}$$

The input impedance of the lower loop Z_{in}^{lower} can be calculated in a similar way and the total input impedance Z_{in} at the feeder could be evaluated. The expressions of the lumped-circuit elements are listed in appendix B. Finally, the theoretical coupling resistance could be calculated in terms of the input impedance Z_{in}:

$$R_c^{cal} = \frac{Z_0}{\text{SWR}} \tag{4}$$

$$\text{SWR} = \frac{1 + |\Gamma_{\text{in}}|}{1 - |\Gamma_{\text{in}}|}, \qquad \Gamma_{\text{in}} = \frac{Z_{\text{in}} - Z_0}{Z_{\text{in}} + Z_0} \tag{5}$$

Z_0 is the characteristic impedance of the coaxial line which feeds the antenna, SWR is the standing wave ratio between the maximum and minimum voltages along the feeding line, Γ_{in} is the reflection coefficient at the feeder. R_c^{cal} could be compared with the experimental coupling resistance R_{c} in equation (1) directly.

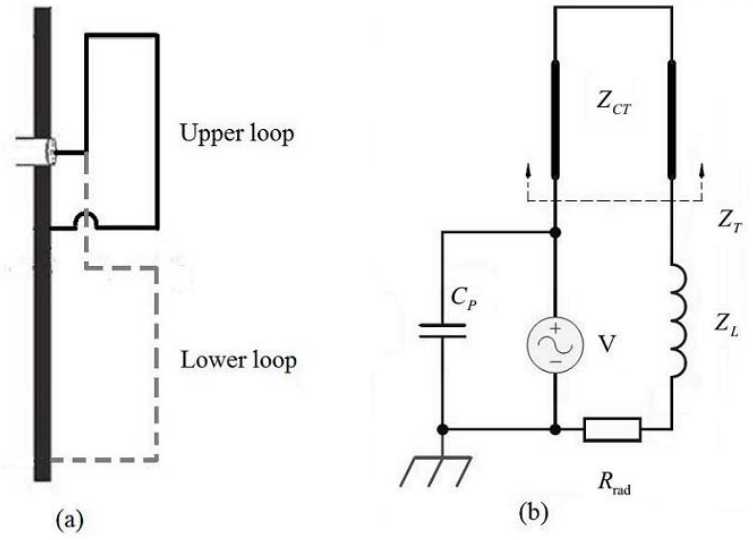

Figure 3. (a) The upper and the lower loop of the ICRF antenna. (b) The lumped circuit model of the upper loop. The transmission line is considered loss-less and lumped resistance R_{rad} at the short point accounts for the radiation. C_P represents the capacitive coupling of the return conductor and the back wall. Z_L gives the inductance of a part of the upper radiation conductor between the feeder and the shorter point.

3. Results

In this section, we will analyze some key factors that influence the coupling characteristics of the I port antenna involving the gap, the electron density, the antenna phasing, the gas injection and the L-H transition in H-minority heating experiments. In order to explain the experiment results qualitatively , the approximate coupling efficiency in [15] was employed:

$$\kappa = \frac{P_{trans}}{P_0} = e^{-1.1 k_{//} L_c} \tag{6}$$

Here, κ is the coupling efficiency, P_{trans} is the power transmitted, P_0 is a constant proportional to the current $\bar{I}^2$ in the antenna, $k_{//}$ is the parallel wave-number and L_c is the width of the evanescent layer. The coupling resistance R_c in equation (1) is the same order of the coupling efficiency κ. So we expect that R_c as a function of the $k_{//}$ or L_c also obeys the equation (6) approximately. The cutoff density of the plasma is calculated by solving the equation:

$$\omega_{pi}^2 \le \omega_{ci}(\omega+\omega_{ci})(\frac{c}{\omega}k_{//})^2 \quad (7)$$

where $\omega_{pi}^2 = n_i e^2/\varepsilon_0 m_i$ is the ion plasma frequency, n_i is the ion density, ω_{ci} is the cyclotron frequency of ionic species (i) and ω is the generator frequency.

The conditions for the experiments were: major radius $\mathrm{R} = 1.88\mathrm{m}$, minor radius $\mathrm{a} = 0.45m$, the radial position of the limiter $R_0 = 2.34m$, plasma current $\mathrm{I_p} = 400 \sim 500\mathrm{kA}$, toroidal magnetic field $\mathrm{B} = 2.2 \sim 2.5\mathrm{T}$, central line averaged electron density $\mathrm{n_{e0}} = 2.5 \sim 4\times10^{19}\,\mathrm{m}^{-3}$, minority hydrogen concentration is around 5-7%. The frequency used is 34MHz in EAST for the minority ICRF regime and total ICRF power is 0.5~2MW.

3.1. Dependence on the gap

We change the mid-plane gap between the plasma limiter and the last closed flux surface （LCFS）by adjusting the center position of the plasma. The antenna is fixed in dipole phasing (0,π,0,π) whose dominant parallel wave number is $|k_{//}| = 13.64$ (as shown later in Figure 6(b)) and the cutoff density is around $\mathrm{n}_{cutoff} = 9\times10^{18}/m^3$. As is shown in Figure 4(a), the coupling resistance R_c decreases with the gap as an exponential function in agreement to the code calculation results. The uncertainty of the experimental results for a gap configuration is $\Delta R_c \sim 0.5\Omega$ which may be caused by the local fluctuation of the plasma density. Figure 4 (b) is the edge electron density profiles corresponding to the gap values in Figure 4(a) measured by the microwave reflectometry. The explanation of this phenomenon is that the rf waves is evanescent in vacuum and in the region where the plasma density doesn't exceed the cut-off density for a certain spectral component. Widening the gap is equivalent to increase the evanescent layer width between the antenna straps and the position of the cutoff density without changing plasma density profile. Furthermore, the coupling efficiency decreases with the gap increasing as an exponential function according to the equation (6).

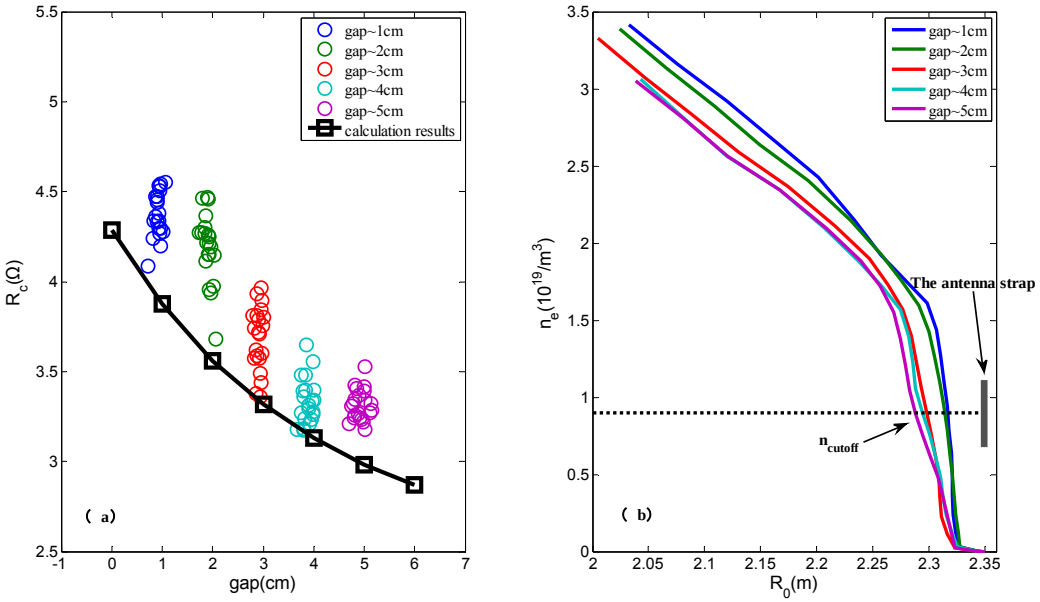

Figure 4. (a) Antenna coupling resistance as a function of the gap between the plasma limiter and the last closed flux surface（LCFS） with (0,π,0,π) phasing. The solid line with black squares denotes the theoretical calculations coming from the variational theory; (b) Edge electron density profiles measured by the microwave reflectometry. The color of the line is the same as the color of the circles in (a) corresponding to a certain gap configuration. The position error ΔR_0 is about 0.3~0.4 cm at the edge while ΔR_0 is about 0.5~0.7 cm in the core region. Dashed line denotes the cutoff density and the position of the antenna straps is $R_0 = 2.36m$.

3.2. Dependence on the central electron density

The experimental and theoretical coupling resistance R_c are both shown to increase with the central line averaged density n_{e0} in Figure 5(a). The antenna phasing is (0,π,0,π) and the gap is 3cm. According to Figure 5(b), the density gradient variation nearby the position of the n_{cutoff} is so little when n_{e0} varying that has almost no influence on the coupling resistance. The resonant behaviour of the coupling resistance due to the variation of the density is also not apparent in phasing (0,π,0,π) [16]. So the key factor to influence the coupling resistance is the radial position of the cutoff density. Increasing the central electron density n_{e0} is equivalent to pushing the position of the cutoff density closer to the antenna and reducing evanescent layer. The growth rate of the experimental coupling resistance is

somewhat higher than the calculation results because we don't take into account of the effect of the increasing density on the gap in the calculation.

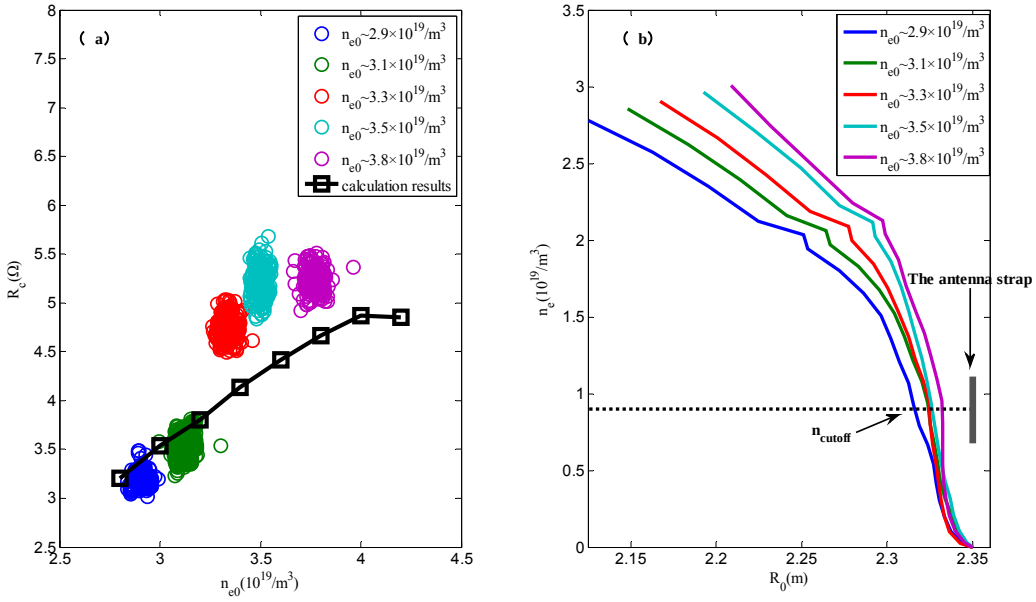

Figure 5. (a) Antenna coupling resistance as a function of the central line averaged electron density with (0,π,0,π) phasing. The solid line with black squares denotes the theoretical calculations coming from the variational theory; (b) Edge electron density profiles measured by the microwave reflectometry. The color of the line is the same as the color of the circles in (a) corresponding to a certain central density configuration. The position error ΔR_0 is about 0.3~0.4 cm at the edge while ΔR_0 is about 0.5~0.7 cm in the core region. Dashed line denotes the cutoff density and the position of the antenna straps is $R_0 = 2.36m$.

3.3. Dependence on the antenna phasing

The coupling resistance with various phasing conditions is displayed in Figure 6(a). On the whole, the experimental coupling resistance is consistent with the calculation results which decreases with the dominant parallel wave number $|k_{//}|$ increasing as an exponential function except for the deviation of the (0,π/2,π,3π/2) phasing case. The current distributions along the poloidal direction as shown in Figure 6(b) with different phasing cases are almost no difference. This eliminates the influence of the poloidal current spectra on the coupling when switching the $k_{//}$. Reducing the $|k_{//}|$ could improve the coupling efficiency directly through $|k_{//}|$ and indirectly by reducing the evanescent width (corresponding to the lower cutoff density) in terms of the approximate coupling efficiency in equation (6). The dominant

parallel wave number $|k_{//}|$ could be read from the normalized toroidal current spectra in Figure 6(c) and (d) corresponding to the different phasing configurations. Two possible reasons may contribute to the deviation of the experimental coupling resistance in (0,π/2,π,3π/2) phasing from the calculation results: distortion of the power spectrum caused by lateral structure and the density modification owing to the RF sheath.

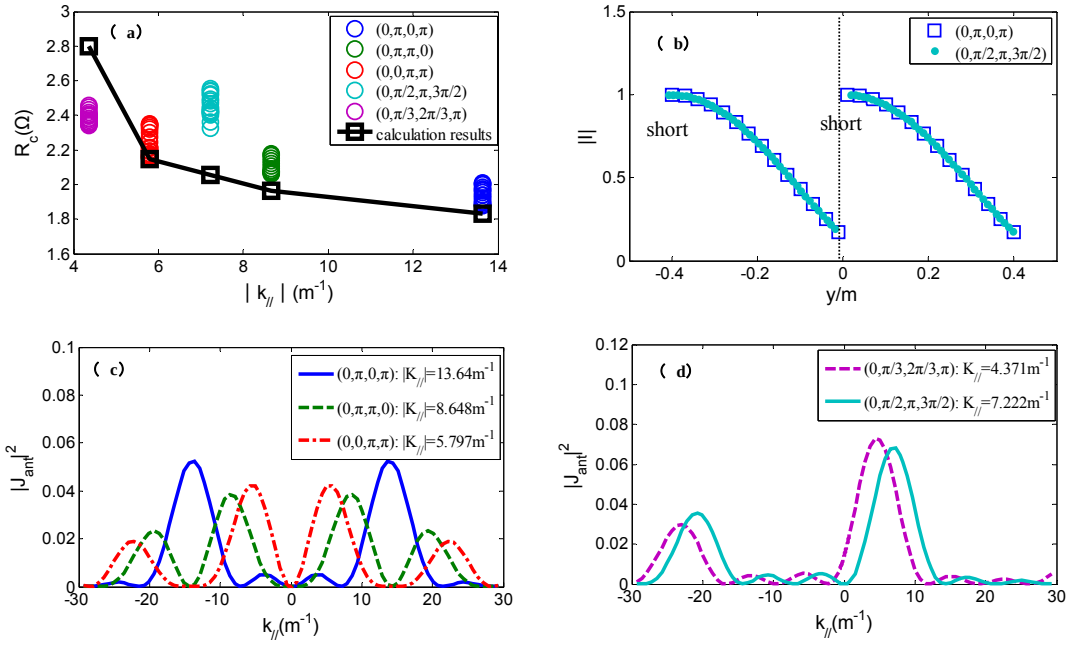

Figure 6. (a)Antenna coupling resistance as a function of the dominant parallel wave number $|k_{//}|$. The solid line with black squares denotes the theoretical calculations coming from the variational theory; (b)the normalized current distributions along the poloidal direction calculated by the antenna code with phasing (0,π,0,π) and phasing (0,π/2,π,3π/2); (c)the normalized toroidal current spectra of three different heating cases; (d)the normalized toroidal current spectra of two different current drive cases. The color of the line is the same as the color of the circles in (a) corresponding to a certain phasing configuration.

3.4. Dependence on the gas injection

The dependence of the relative variation of the coupling resistance on the rate of the injected gas in B port is shown in Figure 7. The antenna in B port operates in dipole phasing. The gas is chosen as deuterium, the plasma current is 400kA, the central line averaged density

n_{e0} is around $3.5\times10^{19}m^{-3}$ and the ICRF power is 1MW. Five gas injectors are placed as uniformly-spaced array from top to bottom at each side limiter of the antenna port. Neither the degradation of confinement nor the variation of the central plasma density was observed for the sake of small amount of the gas injection. The coupling resistance increases with the rate of the injected gas increasing. Injecting the gas in front of the antenna is equivalent to increasing the plasma density in the SOL and reducing the evanescent layer. The coupling resistance increases beyond 35% with the gas injection rate of 3.5×10^{20}/s during the gas injection experiment compared with the resistance without the gas injection.

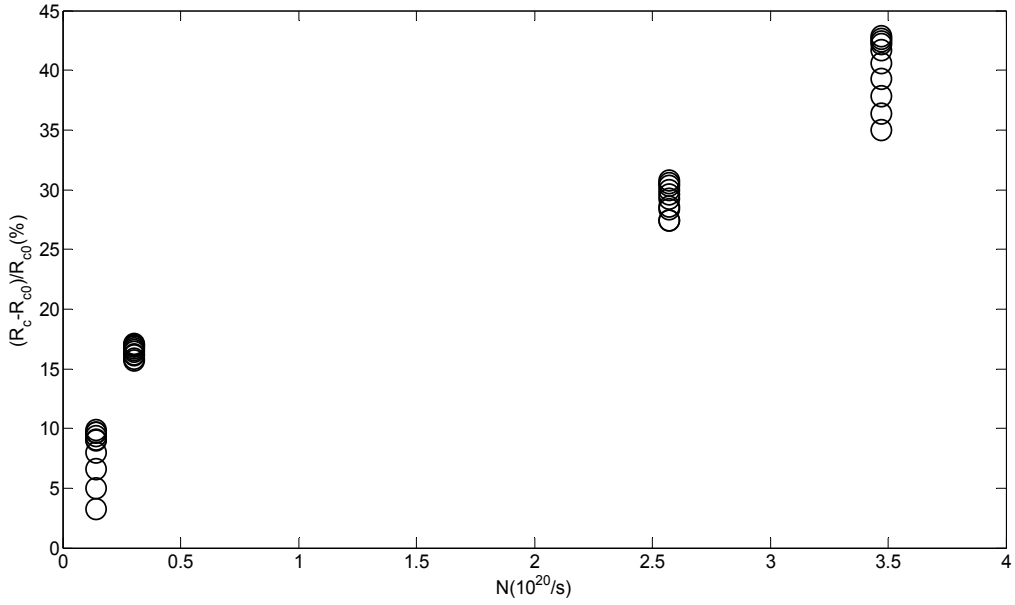

Figure 7. Relative variation of the coupling resistance as a function of the rate of the injected gas in B port. R_{c0} denotes the coupling resistance without the gas injection.

3.5. Coupling during the H-mode

As is shown in Figure 8, a steady H-mode is achieved due to the combination of the auxiliary heating methods including the ICRF, LHW and ECRH. $P_{ICRF}=0.5MW$, $P_{LHW}=3MW$, $P_{ECRH}=0.4MW$ and the steady H-mode lasts about 2 seconds. The antenna phasing is (0,π,0,π). The coupling resistance decreases sharply at the L-H transition due to the marked change in density profile at the SOL [7]. The higher central electron density in H mode (corresponding to the lower density at the SOL) compared with L mode as shown in

Figure 8 (b) occurs because of the transport barrier caused by H mode. Moreover, many positive spikes occur on R_c during the steady H-mode that are coincident with ELMs and the relative variation of the positive spikes of the R_c is beyond 20%. The SOL density decreases at the L-H transition and the spiky changes of the SOL density are caused by ELMs.

Results from an experiment where 2.45GHz low hybrid wave (LHW) power was modulated during an H-mode heated by ICRF power are shown in Figure 9. The ICRF antenna coupling resistance during LHW heating is higher than the resistance without LHW heating because the density in the SOL with LHW is higher as shown in Figure 9(e). We observe no such significant phenomenon during the L-mode when the power and the phasing configurations of LHW are altered. The frequency of the positive spikes consistent with the ELMs is also different between the periods with and without the LHW. This gives us a hint to speculate that the LHW modifies the density profile in front of the ICRF antenna by changing the behavior of the ELMs. More experiments need to be launched to confirm this point.

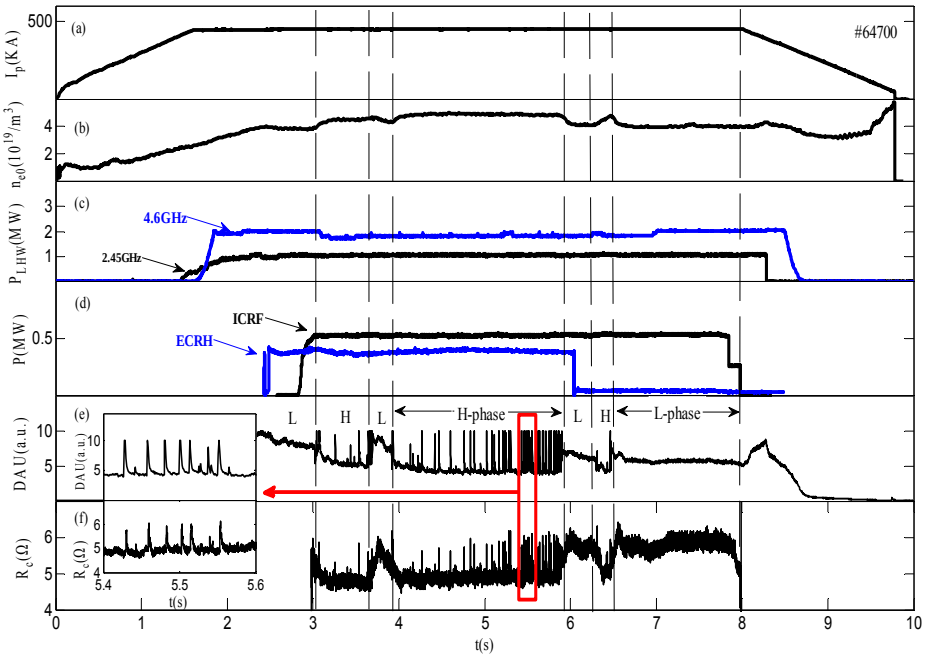

Figure 8. H-mode discharge in 10% H-minority heating experiments. (a) Plasma current, (b) central electron density, (c) LHW power, (d) ICRF power and ECRH power, (e) D_α , (f) antenna coupling resistance in I port.

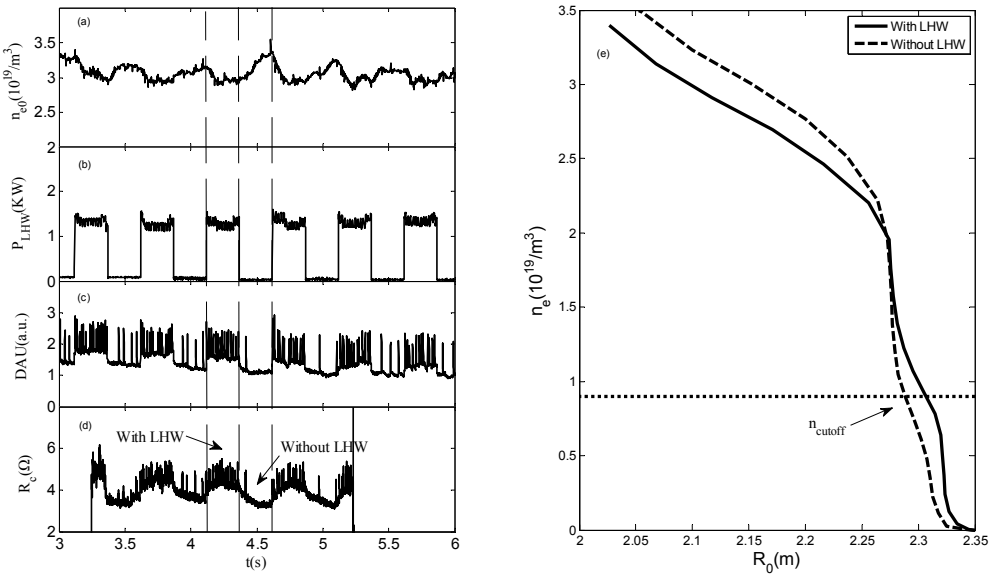

Figure 9. 2.45GHz LHW modulation experiment during the H-mode. (a) Central electron density, (b) modulation power of 2.45GHz LHW, (c) D_α, (d)antenna coupling resistance in I port, (e) edge electron density profiles measured by the microwave reflectometry with and without the 2.45GHz LHW. The position error ΔR_0 is about 0.3~0.4 cm at the edge while ΔR_0 is about 0.5~0.7 cm in the core region.

4. Discussions and conclusions

A series of experiments aimed at improving the coupling of the ICRF antenna have been carried out in EAST tokamak. The experimental coupling resistance is compared with the calculation results which come from the upgraded antenna coupling code based on the variational theory. Rough agreements between the experimental coupling resistance and calculation results are obtained. Either reducing the gap between the limiter and the LCFS or increasing the plasma density can enhance the coupling resistance of the antenna with dipole phasing by adjusting the position of the cutoff density on the low-field-side. Altering the antenna phasing from spectra of higher parallel wave number to spectra of lower parallel wave number can also improve the coupling efficiency significantly regardless of the heating efficiency. During the gas injection experiments, the coupling resistance increases beyond 35% with the gas injection rate of 3.5×10^{20}/s compared with the resistance without the gas injection. The coupling resistance decreases sharply at the L-H transition and the positive spikes of the coupling resistance caused by ELMs have a bad effect on the stability of the ICRF system. However, it is notable that the presence of the LHW can improve the ICRF

antenna coupling efficiency during the H-mode by modifying the density profile in the SOL. The speculation that the LHW modifies the density profile in front of the ICRF antenna by changing the behavior of the ELMs needs to be confirmed in the future.

Appendix A: The antenna coupling code based on the variational theory

Appendix A.1 Derivation of the wave equations for a single antenna.

We normalize Maxwell's equations in the calculations as in Ref.[12]. The subscript 'p' denotes the physical quantity, then: $\boldsymbol{x} = (\omega/c)\boldsymbol{x}_P$, $\boldsymbol{E} = \boldsymbol{E}_P$, $\boldsymbol{H} = (\mu_0/\varepsilon_0)^{1/2}\boldsymbol{H}_P$, $\boldsymbol{J} = (1/\omega\varepsilon_0)\boldsymbol{J}_P$. With these normalizations, expressions for impedance should be multiplied by $(\mu_0/\varepsilon_0)^{1/2} = 377\Omega$ to recover the physical result. We then have Maxwell's equations:

$$\nabla \times \boldsymbol{E} = \mathrm{i}\,\boldsymbol{H} \tag{A1}$$

$$\nabla \times \boldsymbol{H} = \boldsymbol{J} - \mathrm{i}\,\boldsymbol{E} \tag{A2}$$

From Maxwell's equations, the equations for E_z and H_z are:

$$\frac{\mathrm{d}^2 E_z}{\mathrm{d}x^2} - \Gamma^2 E_z = n_z\left(\mathrm{i}\,n_y J_y + \frac{\mathrm{d}J_x}{\mathrm{d}x}\right) \tag{A3}$$

$$\frac{\mathrm{d}^2 H_z}{\mathrm{d}x^2} - \Gamma^2 H_z = -\frac{\mathrm{d}J_y}{\mathrm{d}x} + \mathrm{i}\,n_y J_x \tag{A4}$$

where

$$\Gamma^2 = n_y^2 + n_z^2 - 1 \tag{A5}$$

The current distributions on conductors of the antenna are modeled by:

$$J_y(x,y,z) = J_{y1}(y,z)\delta(x-b_1) + J_{y2}(y,z)\delta(x-b_2), \tag{A6}$$

$$J_x(x,y,z) = J_{x1}(y,z)\gamma(b_1-x) + J_{x2}(y,z)\left[\gamma(b_2-x) - \gamma(b_1-x)\right] + J_{x3}(y,z)\gamma(b_2-x), \tag{A7}$$

where $\gamma(x)$ is the step-function and $\delta(x)$ the Dirac delta. The solution for E_z ($0 \le x \le c$) consistent with the boundary conditions ($E_z(x=0) = E_z(x=c) = 0$) is:

$$E_z(x) = S(x,b_1)n_z\left[\mathrm{i}\,n_y J_{y1} - \left(J_{x1} - J_{x2}\right)\right] + S(x,b_2)n_z\left[\mathrm{i}\,n_y J_{y2} - \left(J_{x2} + J_{x3}\right)\right], \tag{A8}$$

where

$$\mathrm{S}(\mathrm{x},\xi) = \begin{cases} \dfrac{-\sinh\left[\Gamma\left(\mathrm{c}-\mathrm{x}\right)\right]\sinh\left(\Gamma\xi\right)}{\Gamma\sinh\left(\Gamma\mathrm{c}\right)}, \mathrm{x} \geq \xi \geq 0, \\ \dfrac{-\sinh\left[\Gamma\left(\mathrm{c}-\xi\right)\right]\sinh\left(\Gamma\mathrm{x}\right)}{\Gamma\sinh\left(\Gamma\mathrm{c}\right)}, \xi \geq \mathrm{x} \geq 0. \end{cases} \tag{A9}$$

The boundary conditions for H_z are imposed as follows:

$$\frac{\mathrm{d}\,H_z(0)}{\mathrm{d}\,x} = 0, \tag{A10}$$

$$H_z(d) = Y_P(n_y,n_z)\left(-\frac{\mathrm{i}}{1-n_z^2}\right)\frac{\mathrm{d}\,H_z(d)}{\mathrm{d}\,x}, \tag{A11}$$

where Y_P is the plasma admittance defied as $Y_P(n_y,n_z) = \dfrac{1}{Z_P(n_y,n_z)} = \dfrac{H_z(n_y,n_z)}{E_z(n_y,n_z)}$ at $x = d$. The solution for H_z satisfied with satisfying the boundary conditions can be written as:

$$H_z(x) = T(x,b_1)\left[J_{y1} + \frac{\mathrm{i}\,n_y\left(J_{x1}-J_{x2}\right)}{\Gamma^2}\right] + T(x,b_2)\left[J_{y2} + \frac{\mathrm{i}\,n_y\left(J_{x2}+J_{x3}\right)}{\Gamma^2}\right] - \frac{\mathrm{i}\,n_y J_x(x)}{\Gamma^2}, \tag{A12}$$

where

$$\mathrm{T}(\mathrm{x},\xi) = \begin{cases} \dfrac{-\Gamma\cosh\left[\Gamma\left(\mathrm{d}-\mathrm{x}\right)\right] - \rho\sinh\left[\Gamma\left(\mathrm{d}-\mathrm{x}\right)\right]}{\Gamma\sinh\left(\Gamma\mathrm{d}\right) + \rho\cosh\left(\Gamma\mathrm{d}\right)}\sinh\left(\Gamma\xi\right), \mathrm{x} \geq \xi \geq 0, \\ \dfrac{\Gamma\sinh\left[\Gamma\left(\mathrm{d}-\xi\right)\right] + \rho\cosh\left[\Gamma\left(\mathrm{d}-\xi\right)\right]}{\Gamma\sinh\left(\Gamma\mathrm{d}\right) + \rho\cosh\left(\Gamma\mathrm{d}\right)}\cosh\left(\Gamma\mathrm{x}\right), \xi \geq \mathrm{x} \geq 0, \end{cases} \tag{A13}$$

and

$$\rho = \mathrm{i}\left(n_z^2 - 1\right)Z_P\left(n_y,n_z\right). \tag{A14}$$

Having obtained the solutions for E_z and H_z, we can proceed to obtain the other field components through the procedures in Appendix A of Ref.[12] as follows:

$$E_y = \frac{1}{1-n_z^2}\left[-n_y n_z E_z - \mathrm{i}\frac{\mathrm{d}H_z}{\mathrm{d}x}\right], \tag{A15}$$

$$E_x = \frac{1}{1-n_z^2}\left[\mathrm{i}n_z \frac{\mathrm{d}E_z}{\mathrm{d}x} - n_y H_z\right] - \frac{\mathrm{i}}{1-n_z^2}\left[J_x\right], \tag{A16}$$

$$H_y = \frac{1}{1-n_z^2}\left[-n_y n_z H_z + \mathrm{i}\frac{\mathrm{d}E_z}{\mathrm{d}x}\right], \tag{A17}$$

$$H_x = \frac{1}{1-n_z^2}\left[\mathrm{i}n_z \frac{\mathrm{d}H_z}{\mathrm{d}x} + n_y E_z\right]. \tag{A18}$$

Furthermore, the radiation impedance can be written in the variational form as:

$$Z_{\mathrm{rad}} = \frac{2P}{I_{AK} I_{AJ}^*} \tag{A19}$$

where

$$P = \frac{1}{2}\int_D \boldsymbol{K}^* \cdot \boldsymbol{E}(\boldsymbol{J})\mathrm{d}\boldsymbol{R} = \frac{1}{8\pi^2}\int_{-\infty}^{\infty}\mathrm{d}n_y \int_{-\infty}^{\infty}\mathrm{d}n_z \psi(n_y, n_z) \tag{A20}$$

In Equation (19) and (20), D denotes the surface of the central conductors, $\boldsymbol{J}$ and $\boldsymbol{K}$ are the trial functions for the currents, and I_{AJ} and I_{AK} are the total currents flowing at the short point, which are consistent with $\boldsymbol{J}$ and $\boldsymbol{K}$, respectively. The integration could be calculated by using Parseval's theorem and $\frac{\psi}{8\pi^2}$ is the spectral power density.

The condition $\delta Z_{\mathrm{rad}} = 0$ will lead to the physical current $\boldsymbol{J}$ flowing in the conductors and the corresponding antenna radiation impedance Z_{rad} at the short point.

Appendix A.2 Choice of trial functions for a single strap

The current on the conductor in the z direction is assumed to be uniform when the conductors are much longer than wide width and the width is much shorter than a wavelength at the operating frequency. Then

$$\boldsymbol{J}(y,z) = \boldsymbol{J}(y)M(z) \tag{A21}$$

where $M(z) = 1$ on the conductor($|z| \le w/2$) and is 0 otherwise.

In the y direction, a series of cosine functions are employed as trial functions in order to

satisfy continuity conditions at the connections and the short-circuit condition $\frac{\mathrm{d}J_{y2}(y)}{\mathrm{d}y}=0$

at $y=y_1$ and $y=-y_2$.

$$J_{y1}^{(n)}(y)=\cos\left[nk\left(-y+\left|2y_2-y_1\right|\right)\right]\left[\gamma(y-y_F)-\gamma(y-y_2)\right] \\ -\cos\left[nk\left(y+y_2\right)\right]\left[\gamma(y-y_1)-\gamma(y-y_F)\right] \tag{A22}$$

$$J_{y2}^{(n)}(y)=-\cos\left[nk\left(y-y_1\right)\right]\left[\gamma(y-y_1)-\gamma(y-y_2)\right] \\ -\cos\left[nk\left(y+y_2\right)\right]\left[\gamma(y+y_2)-\gamma(y+y_1)\right] \tag{A23}$$

$$J_{x1}^{(n)}(y)=2\cos\left[nk\left(y_F+y_2\right)\right]\delta\left(y-y_F\right) \tag{A24}$$

$$J_{x2}^{(n)}(y)=\cos\left[nk\left(y_2-y_1\right)\right]\delta(y-y_2)+\cos\left[nk\left(y_2-y_1\right)\right]\delta(y+y_1) \tag{A25}$$

$$J_{x3}^{(n)}(y)=-\delta(y-y_1)-\delta(y+y_2) \tag{A26}$$

where $\gamma(x)$ is the step-function $\gamma(\mathrm{x})=0,\ \frac{1}{2},\ 1$ for $x<0,\ x=0,\ x>0$, respectively.

We could express each current in terms of a linear combination of these trial functions:

$$J_{\alpha_1\beta_1}\left(y,z\right)=\sum_{n=0}^{N}a_nJ_{\alpha_1\beta_1}^{(n)}(y)M\left(z\right) \tag{A27}$$

$$K_{\alpha_2\beta_2}\left(y,z\right)=\sum_{n=0}^{N}b_nJ_{\alpha_2\beta_2}^{(n)}(y)M\left(z\right) \tag{A28}$$

Here, a_n and b_n are the coefficients for $\boldsymbol{J}$ and $\boldsymbol{K}$, where $\mathrm{n}=0,\ 1...\mathrm{N}$. $k=1$ is often used though the final radiation impedance Z_{rad} is independent of the values of the *k*.

$N=3\sim4$ is large enough to get a rather small calculation error for Z_{rad}.With these trial functions, the Equation (A19) can be rewritten as:

$$Z_{rad}=\frac{\sum_{m,n}b_mL_{mn}a_n}{\left(\sum_n a_nP_n\right)\left(\sum_m b_mP_m\right)} \tag{A29}$$

where $P_n=2w$ and the matrix elements are as follows:

$$L_{mn}=\sum_{\substack{\alpha_1,\alpha_2=x,y\\ \beta_1,\beta_2=1,2,3}}\iint\frac{\mathrm{d}n_y}{2\pi}\frac{\mathrm{d}n_z}{2\pi}K_{\alpha_2\beta_2}^{(m)*}(n_y,n_z)R_{\alpha_2\beta_2,\alpha_1\beta_1}(n_y,n_z)J_{\alpha_1\beta_1}^{(n)}(n_y,n_z) \tag{A30}$$

Requiring an extremum $\delta Z_{rad} = 0$, we will obtain an radiation impedance at the short point and the physical current coefficients on conductors:

$$Z_{rad} = \frac{1}{\boldsymbol{P} \cdot \boldsymbol{L}^{-1} \cdot \boldsymbol{P}} \tag{A31}$$

$$\boldsymbol{a} = Z_{rad}\left(\boldsymbol{L}^{-1} \cdot \boldsymbol{P}\right) \tag{A32}$$

$$\boldsymbol{b} = Z_{rad}\left(\boldsymbol{P} \cdot \boldsymbol{L}^{-1}\right) \tag{A33}$$

where $\boldsymbol{L} = \left\| L_{mn} \right\|$ and $\boldsymbol{P} = \left(P_0 ... P_N\right)^T$.

Appendix A.3 Extension for the antenna array

The simulations with 4 identical current straps in the toroidal direction can be treated by rewriting the current distribution and resolving Maxwell's equations. The current distribution for the N-strap antenna array can be write as:

$$\boldsymbol{J}_{array} = \sum_{n=0}^{N-1} \boldsymbol{J}\left(x, y, z - n \cdot \Delta z\right) \cdot \exp\left(\mathrm{i}\,\varphi_n\right) \tag{A34}$$

where $\boldsymbol{J}(x, y, z)$ is the current distribution for a single strap antenna, Δz is the period of the antenna array in the z-direction, and φ_n is the current phase of the n-th current strap. If the difference of the radiation impedance between antenna straps is neglected, we can obtain the radiation impedance for each current strap (averaged radiation impedance) by modifying the equation Eq. (A19) into the following expression:

$$Z_{\mathrm{rad}} = \frac{1}{N} \frac{2P_{\mathrm{array}}}{I_{AK} I_{AJ}^{*}} \tag{A35}$$

where

$$P_{\mathrm{array}} = \frac{1}{2} \int_D \boldsymbol{K}_{\mathrm{array}} \cdot \boldsymbol{E}^{*}\left(\boldsymbol{J}_{\mathrm{array}}\right) \mathrm{d}\,\boldsymbol{R} = \frac{1}{8\pi^2} \int_{-\infty}^{\infty} \mathrm{d}n_y \int_{-\infty}^{\infty} \mathrm{d}n_z \psi_{array}(n_y, n_z) \tag{A36}$$

Appendix B: The expression for the lumped-circuit elements

The expression for the lumped-circuit elements in Figure 3 is written as:

$$Z_{\mathrm{L}} = i\omega L_q = i\omega(L + M)(y_F - y_1) \tag{B1}$$

$$Z_T = iZ_{CT} \tan[\beta_T (y_2 - y_F)] \tag{B2}$$

with

$$C_P = C_1(y_2 - y_F) \tag{B3}$$

$$Z_{CT} = \left[(L+M)/(C_1+C_2)\right]^{1/2} \tag{B4}$$

$$\beta_T = \omega\left[(L+M)(C_1+C_2)\right]^{1/2} \tag{B5}$$

where L is the inductance per unit length between the return and radiation conductors, M is the mutual inductance per unit length between the upper and lower loop, C_1 is the capacitance per unit length between return conductors and the back wall, C_2 is the capacitance per unit length between the radiation conductors and the Faraday shield. The value of M is rather small compared with L and often neglected, L, C_1 and C_2 could be estimated in the electrostatic limit:

$$L = \frac{\mu_0(d-b_2)}{w}[\mathrm{H/m}] = 1.257\frac{d-b_2}{w}[\mu\mathrm{H/m}] \tag{B6}$$

$$C_1 = \frac{\varepsilon_0 w}{b_1}[\mathrm{F/m}] = 8.85\frac{w}{b_1}[\mathrm{pF/m}] \tag{B7}$$

$$C_2 = \frac{\varepsilon_0 w}{(c-b_2)}[\mathrm{F/m}] = 8.85\frac{w}{(c-b_2)}[\mathrm{pF/m}] \tag{B8}$$

Acknowledgments

The authors would like to acknowledge the support of the EAST operation and diagnostics group. This work was supported partly by National key research and development program (grant nos 2016YFA0400600 and 2016YFA0400601). This work was supported partly by National Magnetic confinement Fusion Science Programme (grant nos 2015GB101001 and 2013GB106001B). This work was also supported partly by the National Natural Science Foundation of China under grant nos 11675213, 11375235 and 11375236. This work was supported partly by the JSPS-NRF-NSFC A3 Foresight Program in the field of Plasma Physics (NSFC no. 11261140328). Gary Taylor and Joel Hosea are supported at PPPL by US

DoE contract no DE-AC02- 09CH11466. Y. Lin and S. Wukitch are supported at MIT by US DoE contract no DE-FC02-99ER54512.

References

[1] Zhang XJ. *et al* 2013 First results from H-mode plasmas generated by ICRF heating in the EAST *Nucl. Fusion* **53** 023004.

[2] Zhao YP. *et al* 2014 EAST ion cyclotron resonance heating system for long pulse operation *Fusion Eng. Des.* **89** 2642-46.

[3] Nagami M. *et al* 1984 ENERGY CONFINEMENT OF BEAM-HEATED DIVERTOR AND LIMITER DISCHARGES IN DOUBLET-III *Nucl. Fusion* **24** 183-200.

[4] Tanga A. *et al* 1987 MAGNETIC SEPARATRIX EXPERIMENTS IN JET *Nucl. Fusion* **27** 1877-95.

[5] Greenwald M. *et al* 1997 H mode confinement in Alcator C-Mod *Nucl. Fusion* **37** 793-807.

[6] Qin C. *et al* 2015 Electromagnetic Analysis of the EAST 4-Strap ICRF Antenna with HFSS Code *Plasma Sci. Technol.* **17** 167-72.

[7] Mayberry MJ. *et al* 1990 COUPLING OF FAST WAVES IN THE ION-CYCLOTRON RANGE OF FREQUENCIES TO H-MODE PLASMAS IN DIII-D *Nucl. Fusion* **30** 579-97.

[8] Stepanov I. *et al* 2011 Analysis of ICRH antenna loading data in TEXTOR obtained during gas injection experiments *Aip. Conf. Proc.* **1406**.

[9] Parisot A. *et al* 2004 ICRF loading studies on Alcator C-Mod *Plasma Phys. Contr. F.* **46** 1781-92.

[10] Lerche E. *et al* Recent experiments on alternative dipole phasing with the JET A2 ICRF antennas. In: Bobkov V, Noterdaeme JM, editors. Radio Frequency Power in Plasmas. Melville: Amer Inst Physics; 2009. p. 93-96.

[11] Ogawa Y. *et al* 1991 ANALYSIS OF THE LOADING RESISTANCE FOR ICRF HEATING EXPERIMENTS IN ASDEX *Plasma Phys. Contr. F.* **33** 155-68.

[12] Theilhaber K, Jacquinot J. 1984 VARIATIONAL THEORY OF THE ICRH ANTENNA *Nucl. Fusion* **24** 541-54.

[13] Zhang JH. *et al* 2016 Theoretical analysis of the EAST 4-strap ion cyclotron range of frequency antenna with variational theory *Chinese Phys. B* **25** 085201

[14] Maggiora R. *et al* 1998 Electormagtic design of an ICRH system for IGNITOR. *Fusion Engineering and Design.* **38** 353-367

[15] Bilato R. *et al* 2005 Influence of an evanescence layer in front of the antenna on the coupling efficiency of ion cyclotron waves *Nucl. Fusion* **45** L5-L7.

[16] Descamps P. *et al* 1991 Excitation of Global Modes in Textor and Comparison with Theory *Plasma Phys. Contr. F.* **33** 1109-33.